Journal of Structural Geology 133 (2020) 103995

Contents lists available at ScienceDirect

Journal of Structural Geology

journal homepage: http://www.elsevier.com/locate/jsg

Refraction of micro-fractures due to shear-induced mechanical stratigraphy in a low-grade meta-sedimentary rock

Narayan Bose [a], Dripta Dutta [b], Soumyajit Mukherjee [b,*]

[a] Department of Geology and Geophysics, Indian Institute of Technology Kharagpur, Kharagpur, 721 302, West Bengal, India
[b] Department of Earth Sciences, Indian Institute of Technology Bombay, Powai, Mumbai, 400 076, Maharashtra, India

ARTICLE INFO

Keywords:
Deformation mechanism
Rock rheology
Competence contrast
Young's modulus

ABSTRACT

Refracted markers, viz., cleavages and faults, across rock layers are well-documented structural features that develop as the structures propagate through layers of varying competency. We study the Palaeoproterozoic low grade meta-greywacke of the Rautgara Formation, Garhwal Lesser Himalaya, Uttarakhand, India. The focus is on the micro-fractures that cut the flaky-mineral rich cleavage (c-) and the porphyroclast-rich microlithon (m-) domains of the disjunctive foliation planes. Although the rock appears unsheared mesoscopically, in the micro-scale S–C fabric, shadow zones and tails of few quartz porphyroclasts exhibit a top-to-SW ductile shear. A mean kinematic vorticity number (W_m) of ~0.73 has already been determined from this rock. Our renewed study of thin-sections reveal fracture refraction patterns that match with the findings of various known analogue- and analytical models, viz., (i) higher competency contrast between c- and m-domains favours extension fractures over shear fractures, which develop more in the m-domains. Shear fractures dominate in the c-domains, (ii) the angle (Θ) between fracture and the 'layer normal' is higher (>70°) inside the less-competent layers, (iii) a dominant simple shear in the brittle regime produces the P-planes at an angle to the primary shear Y-plane. In one such case, Θ measured from thin-section for 15 successive sub-parallel c-and m-domains show that the most viscous m-domain is ~24 times more viscous than the lowest viscous c-domain. Additionally, out of the eight c-layers, the most viscous c-domain is 3.4 times more viscous than the least viscous c-domain. Similarly, out of the seven m-domains, the most viscous m-domain has a viscosity four times more than the least viscous m-domain. Knowing viscosity ratio of different layers in rocks will enable better analogue and analytical tectonic models. Our numerical models of general shear on linear elastic materials similar to the studied rock type, however, show that the rheological contrast does not influence the curvature of the shear-induced fractures at the boundaries between the quartz-rich sandstone and the mica-rich domains. Close-spaced impurities/notches may curve fracture domains across the layer boundaries producing a 'false' impression of fracture refraction. Moreover, the first principal strain axis (ε_1) does not reorient across the layers except close to the notches. Nevertheless, the current study shows micro-scale development of mechanical stratigraphy under the influence of the ongoing tectonic deformation and quantifies the domain-wise competence contrasts with the help of refracted fractures.

1. Introduction

How far deformation and metamorphism govern rock rheology has been a matter of significant international attention amongst geo-scientists. Such findings are of great use in developing analogue and analytical models for the genesis of structures/deformation of terrains. The term 'competence' qualitatively refers to a material's resistance to deformation. In geological discussions (e.g., Twiss and Moores, 2007), 'competence contrast' usually connotes the competence ratio between the two layers. Several approaches have been made by the previous workers to quantify competence contrast, e.g., using multilayer folding (Huang et al., 2010), use of Schmidt hammer (Katz et al., 2000; Aydin and Basu, 2005), using bone-shaped structure (Kenis et al., 2006). Refraction of markers (cleavages/fractures), the focus of the current study, have also been used as a tool to quantify competence contrast among multiple layers (Ferrill and Morris, 2003; Groome and Johnson, 2006). Refraction of dykes in different scales has also been reported (Fig. 3b of Alsop et al., 2019). Cleavage refraction has been noted across lithologic units for 70 years or more (e.g., Fig. 137A in Nevin, 1949). In ductile regime, cleavage refraction indicates strain compatibility across

* Corresponding author.
E-mail addresses: narayan.bghs@gmail.com (N. Bose), dripta.dutta@gmail.com (D. Dutta), smukherjee@iitb.ac.in, soumyajitm@gmail.com (S. Mukherjee).

https://doi.org/10.1016/j.jsg.2020.103995
Received 20 August 2019; Received in revised form 20 January 2020; Accepted 20 January 2020
Available online 27 January 2020

the layers of different viscosity (Fig. 13.16 in Fossen, 2016). In coarser-grained layers, cleavages develop at higher angles with the bedding (Argles, 2010). Varying orientations of the principal extension axes of the strain ellipsoids across layers of the rock refract the cleavages (review in Price and Cosgrove, 1990), which preferentially develop parallel to the short-axes of the strain ellipsoids (Dennis, 1987).

Likewise, in brittle domain, fault refractions (Fig. 1) have been reported from different rock types, such as carbonates and volcanic rocks consisting of layers (Ferrill et al., 2017a,b and references therein). Study of fractures/faults in different scales constitute an integral part of structural geology and have far-reaching implications in seismicity, basin evolution, petroleum geoscience and orogeny (e.g., Anders et al., 2014; Watkins et al., 2019). Fracture refraction, the cause of the curvature of faults (i.e. listric faults) in multi-layered sequence occurs due to the mechanical stratigraphy, i.e., the compositional difference amongst layers (Weiss, 1972; Hancock, 1985; e.g., field figures in Alsop et al., 2018a, Fig. 2 in Alsop et al., 2018b; possibly Fig. 8c of Alsop et al., 2016; also see Fig. 5.73 of Mukherjee, 2014 for listric fractures cutting across layers). In contrast, fault planes passing almost straight across layers (such as Fig. 6a of Alsop and Marco, 2014) could mean negligible compositional difference of the layers.

Besides mechanical stratigraphy, low confining pressure and low differential stress are also the prerequisites for fracture refraction (Carlini et al., 2019 and references therein). Under the same stress condition, layers with varying competence strain differently (Peacock and Sanderson, 1992). Steep hybrid-/shear-failure are favoured in competent layers, and gently dipping shear fractures in the less competent layers. Shear fractures are more expected in the c-domains, whereas extension fractures in the m-domains (Twiss and Moores, 2007). Higher the competency, greater is the influence of the extension fracture over shear fracture (Treagus, 1988). Least ductile strata fails first and this is followed by the more ductile layers (review in Ferrill et al., 2017a,b). Maccaferri et al. (2010), with the help of mathematical models, show that a crack/dyke deviates towards (or away from) the layer normal when it propagates into a softer/less viscous (or harder/-competent) layer. Hence, the angle between the fracture and the layer normal direction is higher in less-brittle/viscous/competent layer (Treagus, 1983, 1988; Peacock and Sanderson, 1992; Kopp et al., 1994; Ferrill et al., 2017a). Shear fractures make higher angle with the maximum compression direction (angles with layer boundary: shear fractures 20–40°, extension fracture 90°: Ramsey and Chester, 2004). So far, fracture refraction due to mechanical stratigraphy has primarily been studied for normal faults (e.g., Ferrill et al., 2016a; b), with fewer examples for thrusts (e.g., Maillot and Koyi, 2006) and strike-slip faults (e.g., Carlini et al., 2019). In all the cases mechanical stratigraphy has been attributed to the change in lithology in successive beds, through which the fault propagates.

Here we study refracted micro-fractures passing through sheared domains in a naturally deformed low-grade meta-sedimentary rock. The aim is to identify the cause(s) responsible for micro-scale fracture refraction. The competency contrast amongst various domains has been calculated from the angles of refraction of the fractures. The results have been used in a numerical model to understand the role of competence parameters, such as the Young's modulus, behind the competence contrast for elastic materials in micro-scale.

2. Study location & sample description

The study location is at the Gangori Shear Zone (Bose et al., 2018), Inner Lesser Himalaya of the Garhwal region, India. The studied rock sample belongs to the Proterozoic greywacke of the Rautgara Formation (Fig. 2a; Valdiya, 1980, 2010; Célérier et al., 2009; Dubey, 2014; equivalent to the quartz-arenites of the Rautgara Formation of Pant et al., 2012; or the Netala Quartzite of Jain, 1971; Agarwal and Kumar, 1973). Petrographic studies indicate that the rock consists of quartz, muscovite and clay minerals (Fig. 2b). Bose et al.'s (2018) XRD analyses on the clay portion of the rock, and strain analyses of the rock samples reveal that (i) the clays are of clinochlore and illite species; and (ii) a mean Kinematic Vorticity Number W_m of ~0.73 denoting 57% simple shear and 43% pure shear, respectively. A general shear/sub-simple shear regime is expected since such a regime has already been worked out from several other terrains in the Himalaya (e.g., Grasemann et al., 1999; Vannay and Grasemann, 2001; review in Fig. 8 of Mukherjee, 2013).

Under an optical microscope, the rock displays dominantly a disjunctive rough foliation (resembling Fig. 11.3 of Twiss and Moores, 2007, Fig. 3). We choose three refracted fractures (Figs. 3 and 4) from the XZ-section of the rock. Quartz fills up the opening-mode (Mode-1) micro-cracks as cement. Presence of such cement along with the absence of crack-seal texture indicates that the fracture generated in a single event (Trepmann and Stockhert, 2009; Hooker et al., 2018). Inclusion trails and cross-cut relation with newly formed muscovite indicate the quartz vein is syn-kinematic. The shear sense is identified by observing the sigmoidal shear planes and tails/shadow zones associated with the elliptical quartz porphyroclasts. Secondary quartz fills up the irregular fractures with up to ~1.3 mm aperture that cut across other quartz grains (Fig. 3b) as well as the m-domains (Fig. 3c). The following section deals with the estimation of competence contrast from these refracted fractures.

3. Quantification of competence contrast from fracture refraction

Cleavage refraction (Treagus, 1973; Helmstaedt and Greggs, 1980) has been studied extensively through various techniques, e.g., on natural samples (Kanagawa, 1993), in analogue models (Treagus, 1999) and in analytical studies (Treagus, 1983, 1988). From theoretical and analogue models on cleavage refraction, Treagus (1999) propose the following

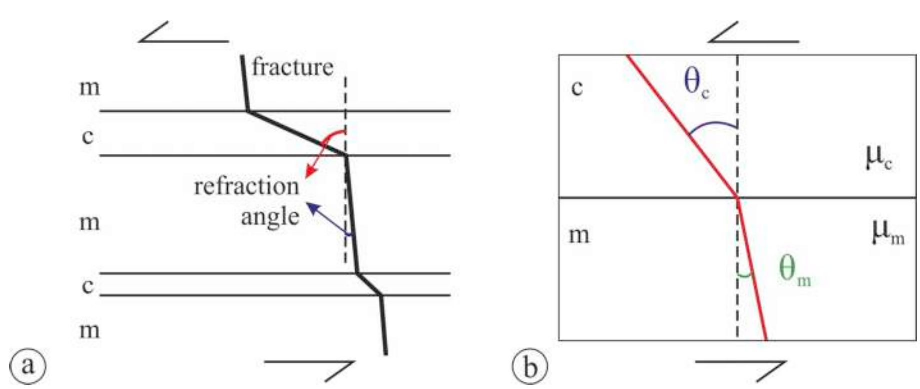

Fig. 1. Schematic diagram: refraction of shear-generated fracture in cleavage (c) – microlithon (m) domains.

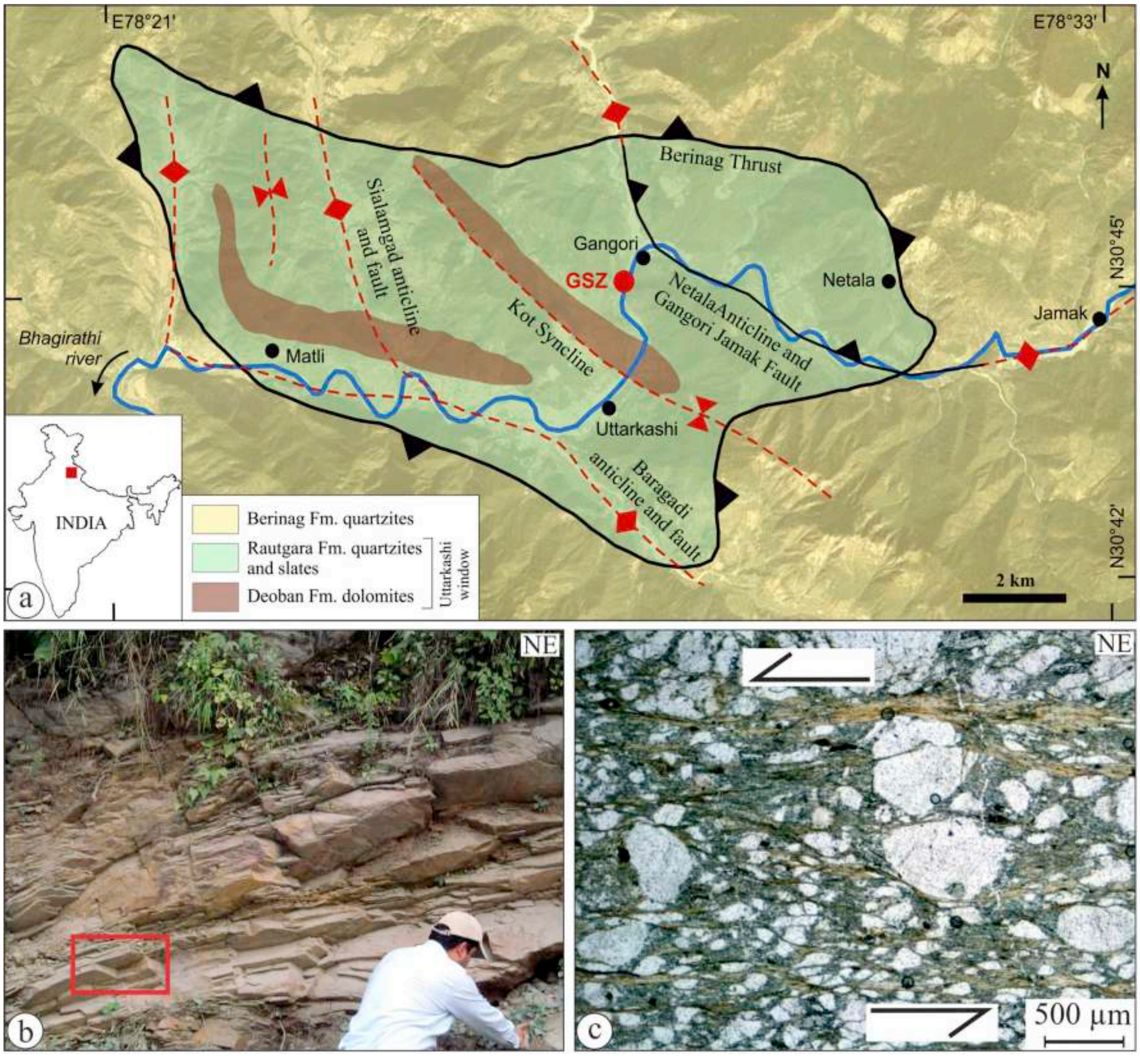

Fig. 2. **(a)** Geological map showing the study location, the Gangori Shear Zone (reproduced after Fig. 1 of Bose et al., 2018). **(b)** Rautgara Formation greywacke exposed at the Gangori Shear Zone (30°45.114′N, 78°27.189′E). Red box: spot of sample collection. S. Mukherjee as scale (~80 cm height visible in the image). **(c)** Micro-texture. The shear planes are rich in clays and indicate the overall top-to-SW slip. Plane polarised light. (For interpretation of the references to colour in this figure legend, the reader is referred to the Web version of this article.)

equation to quantify the competency contrast of the two adjacent domains, which is followed by the subsequent workers for different rock/mineral layers (e.g., Ragan, 2009).

$$\frac{\gamma_c}{\gamma_m} = \frac{\tan\theta_c}{\tan\theta_m} = \frac{\mu_m}{\mu_c} = K(say) \quad (1)$$

γ: shear strain of the domain, θ: the angle between the fracture and the layer normal, μ: dynamic viscosity of the domain; Subscript m: m-domain; c: c-domain.

We measure refraction angles for the three fractures (Fig. 5a and b) and calculate the competency ratios (Fig. 5c) following eqn. (1). Fig. 6 presents graphically the relationship between the thickness of the c- and the m-domains (178–3316 μm thick) versus the refraction angles that range 3–47°. Fig. 6 with the plot of thickness of the two domains vs. the refraction angles shows that the c-domains preferably have lower domain-thickness and higher refraction angle than those of the m-domains. Fig. 7 compares layer-to-layer competency ratios. The figure shows that the m-domains have high competency contrast when compared with a particular m-domain for the chosen fracture. On the other hand, competence contrast amongst the c-domains themselves are much less when compared with a single c-domain for the chosen fracture.

4. Competence parameters and fracturing of brittle material

The rheology of the ductile crust depends on thermal profile, enthalpy input, orogenic architecture and bulk composition etc. (Brown, 2005). The three key parameters indicating rock competence are Young's Modulus (E), compressive strength, and the bulk density (Katz et al., 2003). While viscosity has been widely used as a competence indicator for viscous materials, E has been considered as a gauge of rock stiffness/rigidity/competence for elastic/elasto-viscous materials (e.g., Tsuchiya et al., 2005; Henk and Nemčok, 2008; Jeng and Huang, 2008; Ferrill et al., 2016; 2017b; McGinnis et al., 2017). Studying the growth of fault in multilayer through numerical modelling, Nespoli et al. (2019) report that the crack grows in the direction of maximum energy release. They also report the deflection of crack (or, fault) at the interface of contiguous layers with different rigidity (depends on the Young's modulus and Poisson's ratio). However, the authors found an increase in dip angle of the fault upon entering a softer layer (i.e., lower rigidity).

Referring Young's modulus (E) as the indicator of layer competence, the numerical model by Damasceno et al. (2017) keep the E of competent layer 10 times more than the incompetent layer. They maintain the same Poisson's ratio for layers with variable competence. This is because the Poisson's ratio does not severely affect the deformation mechanism

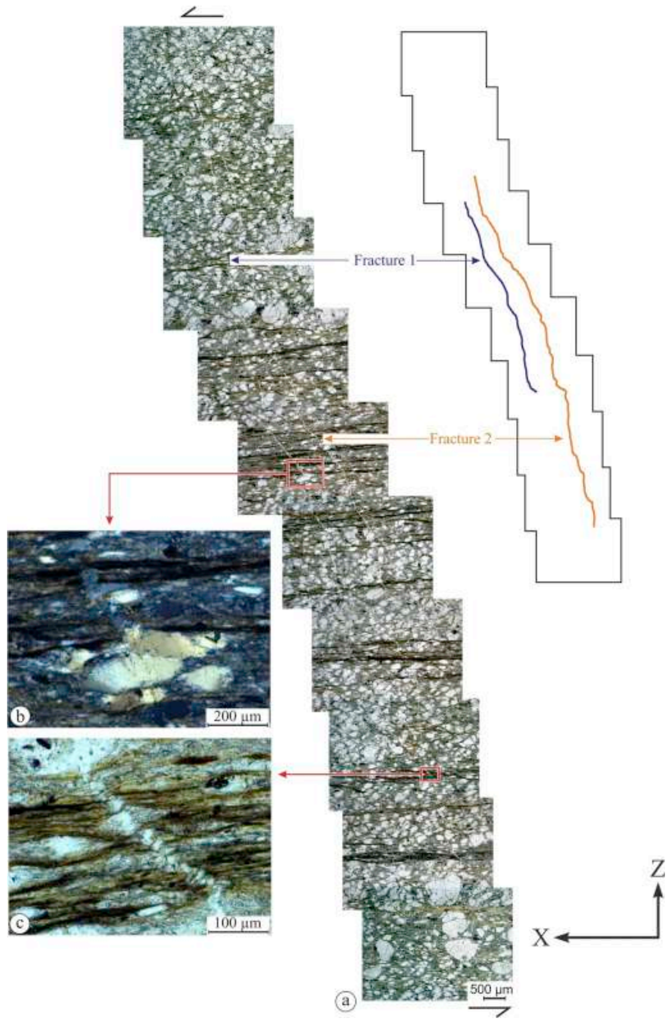

Fig. 3. (a) Mosaic shows two fractures, 1 and 2, passing through several cleavage (c) and microlithon (m) domains. Inset cartoon: extent of the corresponding fractures. Plane polarised light. **(b)** Zoomed part of (a): the nature of fracture-1 passing through quartz porphyroclasts. Cross-polarised light. No drag near the fracture. **(c)** Zoomed part of (a), showing the nature of fracture-2 passing through the clay-rich cleavage domain. Plane polarised light. Minor drag (?) along the fracture.

(Huang et al., 2010). Increase in E decreases the amount of extensional strain for failure (Gross et al., 1995). Bürgmann et al. (1994) check the influence of variable E on the slip along a fault. Koehn et al. (2005) report that the spacing of extension fractures reduces as E elevates. Eyinla and Oladunjoye (2014) consider E as one of the key parameters while predicting the mechanical competency for hydrocarbon exploration.

In place of Young's modulus (E), an "equivalent Young's modulus" ($\overline{E}$) has also been used (e.g., Huang et al., 2010):

$$\overline{E} = E/\left(1 - \upsilon^2\right) \tag{2}$$

here υ: Poisson's ratio.

Due to its sensitivity on pre-existing flaws (e.g., cracks, porosity), the effective Young's Modulus correlates the textural variations with the strength variations (Austin and Kennedy, 2005 and references therein):

$$\sigma_p = aE_{eff}^{b}\sigma_3^{c} + C_o \tag{3}$$

here σ_p: peak differential stress, E_{eff}: effective Young's modulus, σ_3: least principal (compressive) stress, C_o: unconfined compressive strength, and a, b, c: fit parameters.

From lab experiments and finite element studies, Teufel and Clark (1981) deduce that in layered rocks, the layers with higher shear moduli experience more horizontal compression that influences the vertical propagation of hydraulic fracture. Decrease in the effective Young's modulus initiates cracking (Berry, 1960a) by reducing both the stress level and driving force for crack propagation (Berry, 1960b). Strain-rate influence fracture initiation stress (Kipp et al., 1980). Young's modulus, and therefore the effective Young's modulus, decreases with increasing grain-size (Eberhardt et al., 1999).

At all deformation temperatures, fractures originate from the pores/pore agglomerates present at the grain boundaries (Adams et al., 1997). Fractures grow incrementally and interact mutually (Hooker et al., 2018). Mecholsky et al. (1976) find the relation of Young's modulus with the critical flaw sizes and critical fracture energy, which again is governed by microstructures. While experimenting with aluminium metal-matrix composite, Manoharan and Lewandowski (1990) find that influence of microstructures on fracture initiation and growth is much faster in composite materials than on the monolithic materials.

5. Numerical simulations

We perform the 2D-finite element models of linear elastic material with pre-existing impurities/notches, and its response to general shear. In this time-dependent model the stresses/loads on the material boundaries increase non-linearly with time. These simulations are carried out using the software COMSOL Multiphysics v5.4 (2019). Our primary interests are to: (i) observe the temporal evolution of fracture geometry, within and across various layers, (ii) comment on the possible role of competency contrast among layers with regard to (i), and (iii) compare the resulting features with real microstructures (such as Fig. 3).

5.1. Governing equations & other issues

The set of equations to be solved to determine the state of stress and displacements at the end of a time-dependent 2D deformation of an isotropic and linear elastic material are:

$$\rho\frac{\partial^2 u}{\partial t^2} = \nabla \cdot \sigma + F_V \tag{4}$$

$$\sigma = \sigma_0 + C : (\varepsilon - \varepsilon_0 - \varepsilon_{th}) \tag{5}$$

$$\varepsilon = \frac{1}{2}\left[\nabla u + (\nabla u)^T\right] \tag{6}$$

here ρ: density; t: time; u: displacement vector that points from the reference position to the current position such that x = X + u (X,t) (x and X: spatial and material coordinate vectors, respectively); F: body force; σ_0 and ε_0: initial stress and the strain states, respectively; ε_{th}: thermal strain; σ (stress matrix) = $\begin{bmatrix}\sigma_{xx} & \sigma_{xy}\\ \sigma_{yx} & \sigma_{yy}\end{bmatrix}$; ε (strain matrix) = $\begin{bmatrix}\varepsilon_{xx} & \varepsilon_{xy}\\ \varepsilon_{yx} & \varepsilon_{yy}\end{bmatrix}$; C (also written as C_{ijkl}) is the 4th order elasticity tensor that (because of symmetry) can also be represented as a 6 × 6 matrix D. $D = \frac{E}{(1+\nu)(1-2\nu)}$ (E and ν: Young's modulus and Poisson ratio, respectively); ':' = the double-dot tensor product; ∇u (displacement gradient) = $\begin{bmatrix}\frac{\partial u}{\partial X} & \frac{\partial u}{\partial Y}\\ \frac{\partial v}{\partial X} & \frac{\partial v}{\partial Y}\end{bmatrix}$ (always calculated with respect to the material coordinates x, y; Karato, 2008; Gerya, 2010; Qi et al., 2018).

Lab experiments by previous researchers reveal that not only the strength of the rock increases with the intermediate principal compressional stress (σ_2; when $\sigma_1 > \sigma_2 > \sigma_3$) up to a certain value followed by a decrease, but the fault angle (angle between σ_1 and the fault normal) for a normal fault also increases with σ_2 (Mogi, 2007; Haimson et al., 2017). Pan et al. (2012) report that the increase in rock

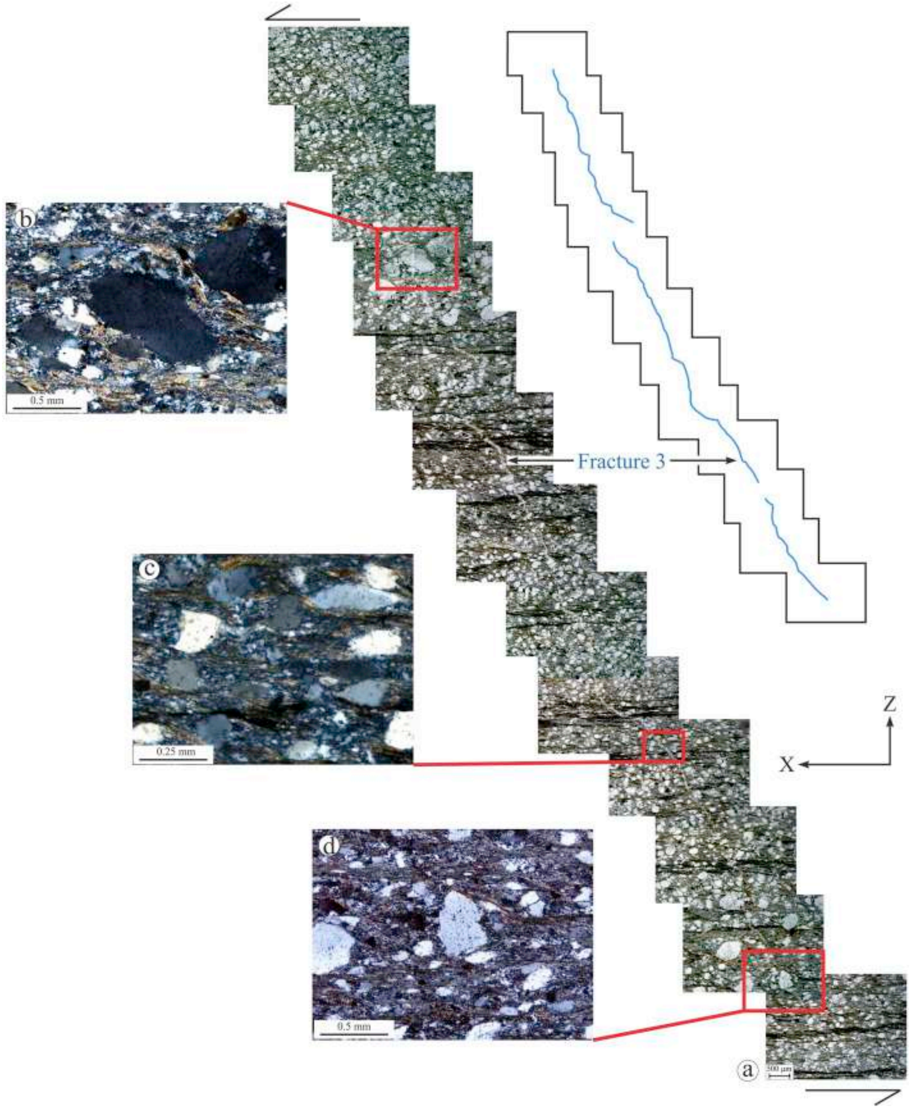

Fig. 4. **(a)** Mosaic shows Fracture 3 passing through cleavage (c) and microlithon (m) domains. Inset cartoon: extent of the corresponding fractures. Plane polarised light. **(b)** Zoomed part of (a): the nature of fracture-3 passing through a quartz porphyroclast. Cross-polarised light. The grain remains uninfluenced by the fracture. **(c)** Zoomed part of (a), showing the nature of fracture-2 passing through the clay-rich cleavage domain. Plane polarised light. Minor drag (?) present along the fracture. **(d)** Zoomed part of (a) showing another example where Fracture 3 is passing through a quartz grains. Note the nature of Fracture-3 before and after interacting with the quartz grain.

strength/failure strength arises due to delayed failure in a moderate σ_2 condition. However, after studying the Shirahama sandstone and the Yuubari shale (Japan) Colmenares and Zoback (2002) show that the failure strength does not strongly depend on the rock composition. Secondly, the failure criteria such as the Mohr-Coulomb or the Hoek-Brown, which do not consider the influence of the intermediate principal stress (σ_2), can be used. The Mohr-Coulomb failure criterion for plane strain deformation of an incompressible linear elastic material is:

$$\tau = C + \mu_i \sigma_n \tag{7}$$

In other words,

$$\sigma_1 \left\{ \sqrt{(1+\mu_i^2)} + \mu_i \right\} - \sigma_3 \left\{ \sqrt{(1+\mu_i^2)} - \mu_i \right\} - 2C = 0 \tag{8}$$

here σ_1: maximum principal stress; σ_3: minimum principal stress; μ_i: coefficient of internal friction, and C: cohesion (Jaeger et al., 2009; Meyer et al., 2017). As demonstrated in Bose et al. (2018), Eqn (8) also represents the condition for brittle failure. Eqn (8) is the Yield Function (Y_F) indicating that fractures develop at locations wherever it is satisfied.

The second invariants of deviatoric stress and elastic strain tensors are given by:

$$(J_2)_{\text{dev.stress}} = \frac{(\sigma_2 - \sigma_3)^2 + (\sigma_1 - \sigma_2)^2 + (\sigma_3 - \sigma_1)^2}{6} \tag{9}$$

$$(J_2)_{\text{elastic strain tensor}} = (J_2)_{\text{elastic strain tensor}} = \varepsilon_{xy}^2 - \varepsilon_{xx}\varepsilon_{yy} \tag{10}$$

$$\varepsilon_1,\ \varepsilon_2 = \frac{\varepsilon_{xx} + \varepsilon_{yy}}{2} \pm \left[\varepsilon_{xy}^2 + \frac{(\varepsilon_{xx} - \varepsilon_{yy})^2}{4} \right] \tag{11}$$

ε_1 and ε_2 are the maximum and minimum principal strains, respectively (Jaeger et al., 2009; Hobbs and Ord, 2015).

5.2. Model set up

We run two categories of 2D-models viz., (a) sandstone layers only (M1) and (b) two non-schistose sandstone layers separated by a layer of mica-schist (M2) (Fig. 7). Although the actual rock type, i.e., greywacke, has also been used in numerical modelling (e.g. McNamara et al., 2014; Mielke et al., 2016), here we use two distinctly different lithologies to address the issue of c- and m-domains with variable competency (Table 1). Each of the two models are sub-divided into three classes based on the location of the notches. A notch represents an impurity/imperfection/flaw/weak zone from where fractures originate (e.g., Wall, 2002; Justo et al., 2017). Notches trigger fracturing in the model.

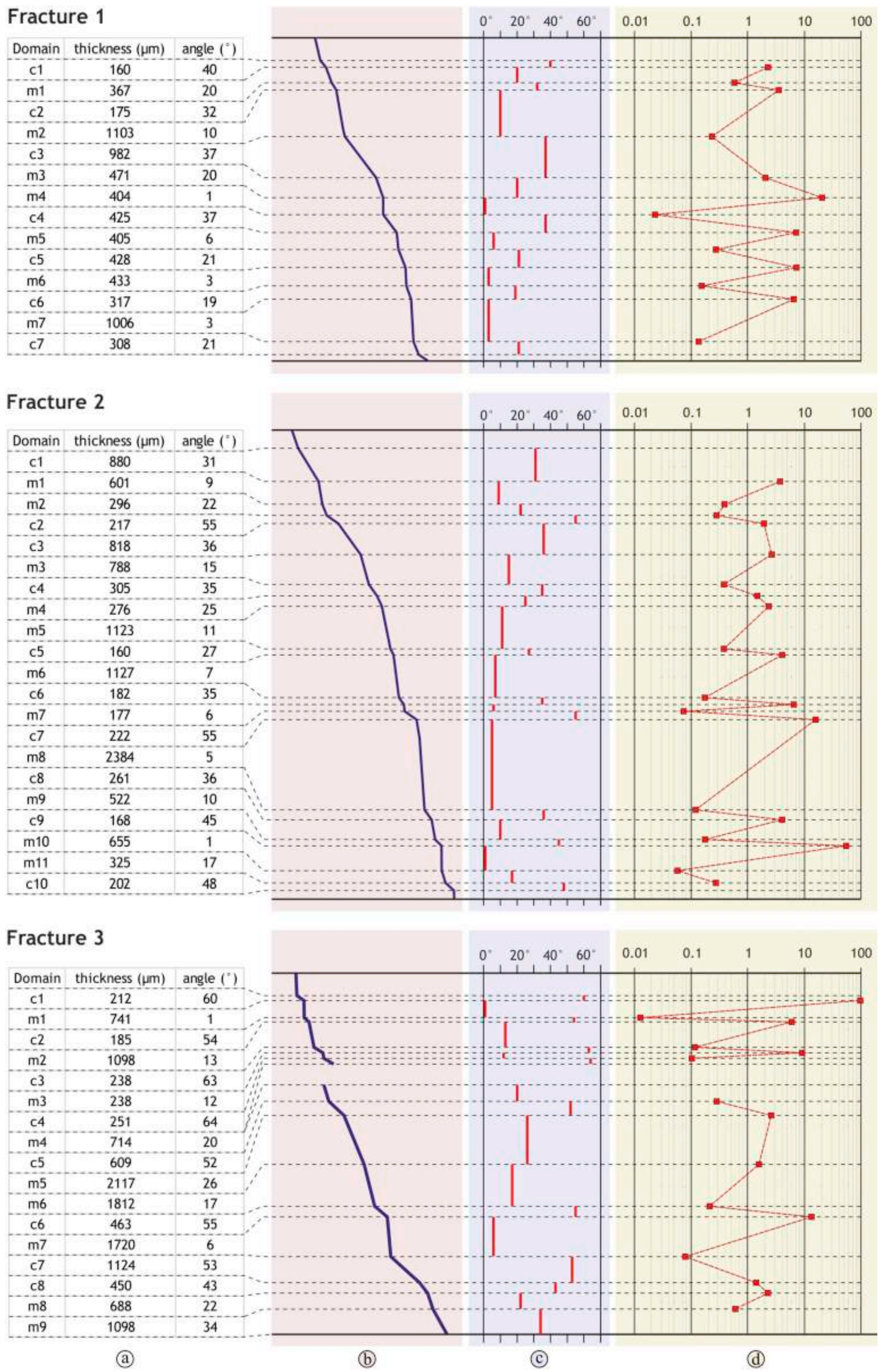

Fig. 5. **(a)** Demarcation of the cleavage (c)- and microlithon (m)-domains in each of the three fractures along with the corresponding domain thickness and refraction angle. **(b)** C- and m-domains are marked on the line drawings of fracture-1 and -2. **(c)** Angle between fracture and layer normal direction in each of the c-m domains. **(d)** Competency contrast between two adjacent layers. Values of the red boxes at domain boundaries indicate ratio of viscosity of lower domain to the upper one, calculated based on eqn (1) in Section-3. Red broken line shows their changing pattern. (For interpretation of the references to colour in this figure legend, the reader is referred to the Web version of this article.)

This is a standard procedure in numerical models (e.g., Virgo et al., 2016; Shovkun and Espinoza, 2019).

The four classes of models are (Figs. 8 and 9): M1-T (T: notches present only in the top layer), M1-M (M: notches present only in the middle layer), M1-B (B: notches present only in the bottom layer), M1-A (A: notches present in all the layers). We have included four notches, three rectangular and one elliptical, in each layer (Fig. 9). In both the models (M1 & M2), (Fig. 8), the top, the middle and the bottom layers are referred to as L_T, L_M and L_B, respectively (Fig. 9). E_T, E_M and E_B are their respective Young's moduli (E) (Fig. 9). In M1 and M2 all the physical properties of the sandstone layers are taken identical except the E i.e., for M1, E_T: E_M: $E_B = 3.5{:}2.5{:}1$; and for M2 $E_T{:}E_B = 3.5{:}1$ (L_M is mica schist in M2 such that $E_M{:}E_B = 1.5{:}1$). These ratios are chosen on a trial-and-error basis for which the fractures turn out to be most prominent.

Each domain/layer has a dimension of $1 \times 0.25\ \mu m^2$. The coordinate

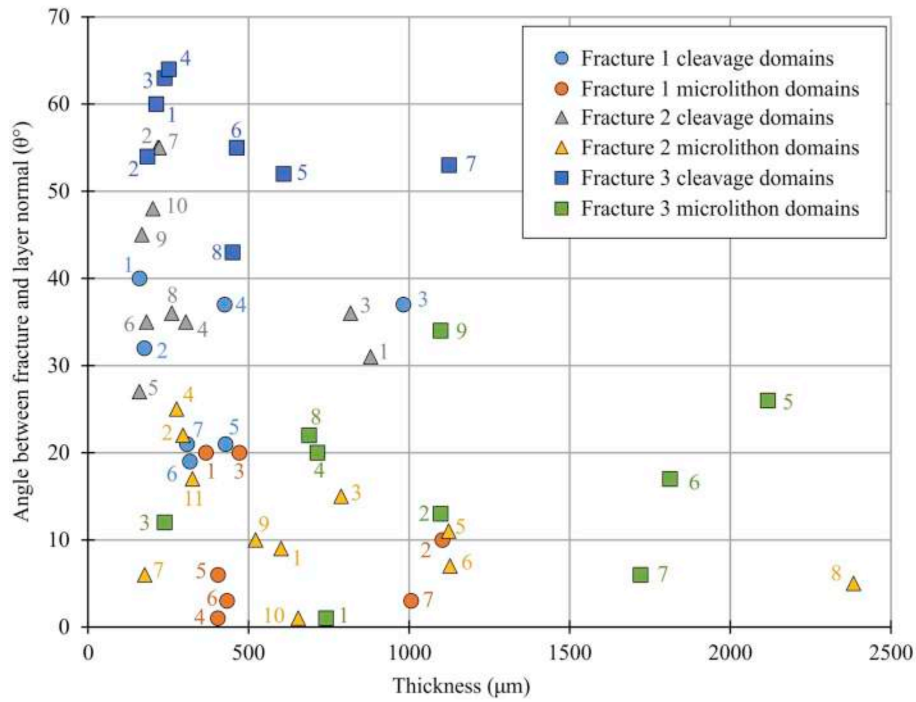

Fig. 6. Relation between domain thickness and refraction angle (θ).

axes x and y are horizontal and vertical, respectively (Fig. 9). Two different kinds of notches have been incorporated viz., rectangular (dimension: 5×10^{-3} μm × 4×10^{-2} μm) and elliptical (major axis: 6×10^{-2} μm, minor axis: 2×10^{-2} μm; i.e., aspect ratio = 3). The dimension of the notches is kept deliberately much smaller than the chosen rectangular domain. However, they are not made very small in order to keep them visible in the figures. A reason of using notches of different geometries and orientation was to understand whether notch geometry itself can influence our results. The rectangular notches are either perpendicular or at an angle, either 50° or 70°, to the x-axis. The major axis of the elliptical notches always parallels the y-axis. Meshing in terms of equilateral triangles with sides of lengths ranging from 3.7×10^{-2} to 0.012×10^{-2} μm has been employed using the mesh generation module in COMSOL with an advancing front tessellation (as in Marques et al., 2005; Johnson et al., 2009; Lo, 2015).

The models are subject to general shear with the ratio of stress responsible for simple shear and pure shear increasing non-linearly with time (Fig. 10) in a plane strain deformation regime. We chose general shear to deform the model layers since our studied samples in thin-section revealed general shear in our previous study i.e., Bose et al. (2018). The shear stress σ_X acts parallel to the x-axis and the interlayer boundaries, whereas the compressive normal stress σ_Y parallels the

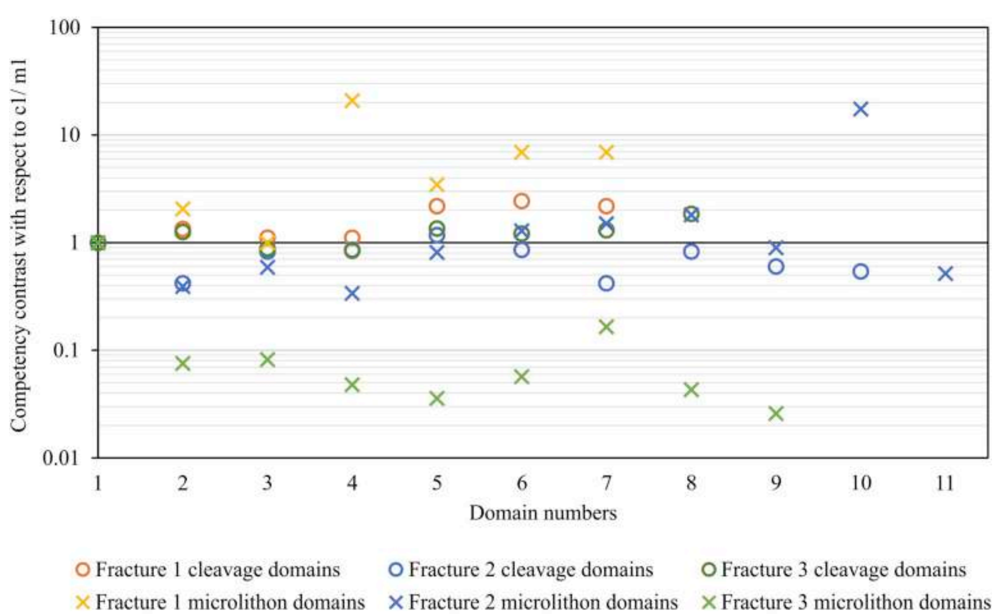

Fig. 7. Comparison of relative competency among the microlithon (a) and cleavage (b) domains. The competency contrast is as per eqn (1) in Section 3. Note that the y-axis is in log scale.

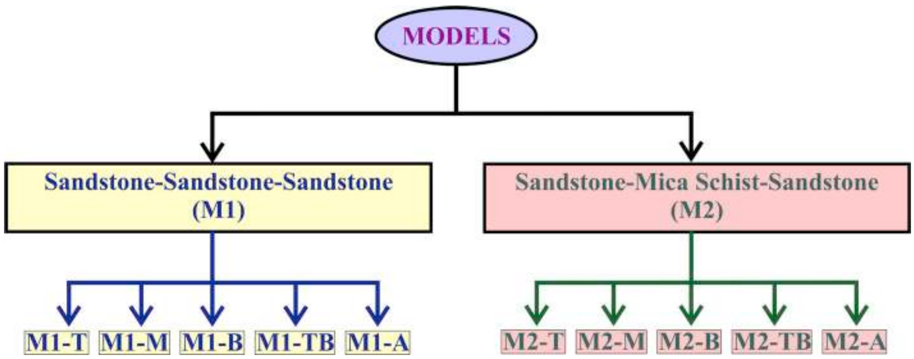

Fig. 8. Types of numerical models in this study.

Table 1
Physical parameters of the materials used in the model in Section 5.2. **References:** 1. Gudmundsson (2011); 2. Henderson and Henderson (2009); 3. Zhang et al. (2008); 4. Goodman (1980); 5. Nasseri et al. (2003); 6. Pollard and Fletcher (2005); 7. Agliardi et al. (2014); 8. Takahashi and Tanaka (2017).

Material	Density[1, 2] (kg m $^{-3}$)	Young's Modulus (GPa)	Poisson's Ratio (unitless)	Cohesion/ Inherent shear strength (MPa)	Angle of Internal friction (radian)
Sandstone	2000-2800[1, 2]	10-60[1, 2]	0.1–0.3[1, 2]	25.5–27.2[3, 4]	0.46[1, 6]
Mica-schist	2500-2700[1, 2]	5–27[5,7]	0.3[1]	19 [4, 8]	0.41[1, 6]

y-axis i.e., acts perpendicular to the interlayer boundaries (Fig. 9). No velocity boundary condition (U_Y = 0) applies on all the domain boundaries except the two that separate the middle layer from the one above and below it (Fig. 9). This is done to inhibit deformation-induced rotation (about an axis directed towards the observer) of the domains. The magnitudes of $|\sigma_X|$ and $|\sigma_Y|$ for model M1 increase non-linearly from 0 to 22.5 MPa and 15 MPa, respectively, whereas for model M2 they rise from 0 to 17.5 MPa and 7.5 MPa in a similar way (Fig. 10). For both the models, the rise in the magnitudes of the applied normal and shear stresses occurs over an interval of 2 s (t = 0 to t = 2 s) (Fig. 10). Whether stress increases temporally is difficult to check in natural examples of fracture refraction cases. We choose to do so in our models as increasing the stress over time resulted in faster growth and better visualisation of the fractures.

5.3. *Results & interpretations*

The most prominent observation of the two models M1 and M2 are the genesis of the two sets of near-straight fractures (zones with $Y_F \geq 0$), one at high-angle (76–85°) and another at much lower angle (15–19°) to the inter-layer boundaries (i.e., the length side), from the ends of the notches (Fig. 11). Also, the orientations of the two sets of fractures in any one of the layers are near similar to that in the other layers i.e. no refraction, which apparently have different values of Young's Modulus (E). The varying competency of the layers (due to different values of E) does not seem to control the nucleation locations of the fractures i.e., no major deflection of fractures across the layers is observed. This holds when notches are present in a single layer (Fig. 11a–i). Another crucial point is that close-spaced notches can cause fractures to deflect (see Model M1-A in Fig. 11).

In the final results of the models M1-T and M1-M (Fig. 11b, n), notice that the fractures originating from the notches nr3 and nr6 are almost straight (Fig. 11e–h). Whereas in M1-A, the fracture at the exact same

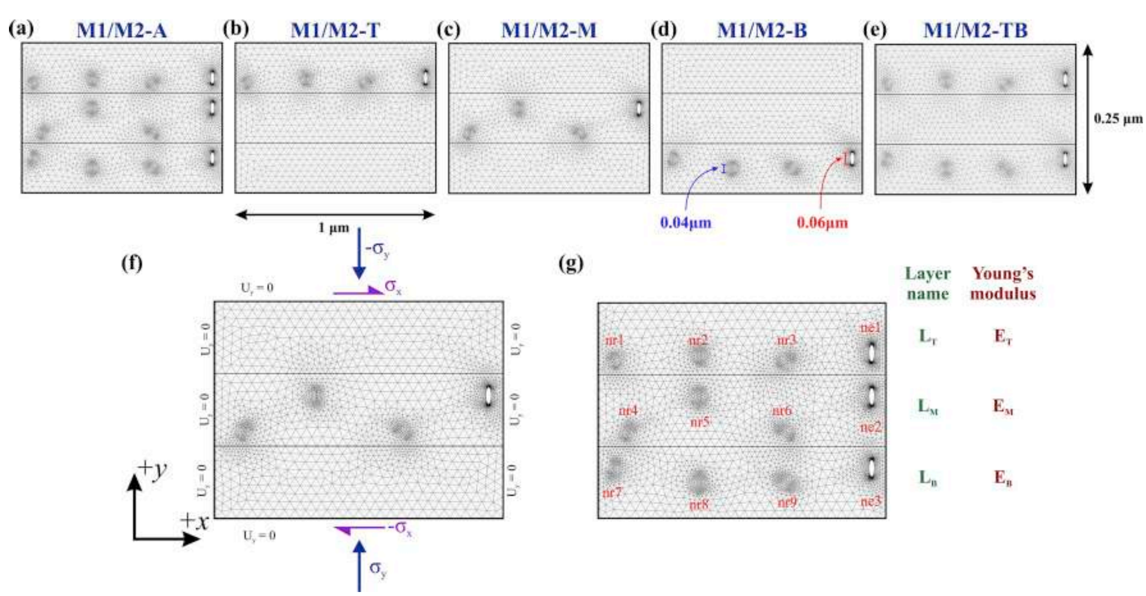

Fig. 9. Geometric parameters, meshing and other nomenclature. We took curvature factor = 0.25, and maximum element growth rate = 1.25. The rectangular and the elliptical notches are incorporated in various combinations viz. **(a)** in all the layers, **(b)** top, **(c)** middle, **(d)** bottom, and (e) both top and bottom layers. All the layers are 1 µm long. The combined width of the three layers is 0.25 µm. **(f)** Sense of the applied stress. **(g)** The names of each of the notches and layers are shown, alongside the Young's modulus for the layers. T, M, and B: top, middle and bottom layers, respectively.

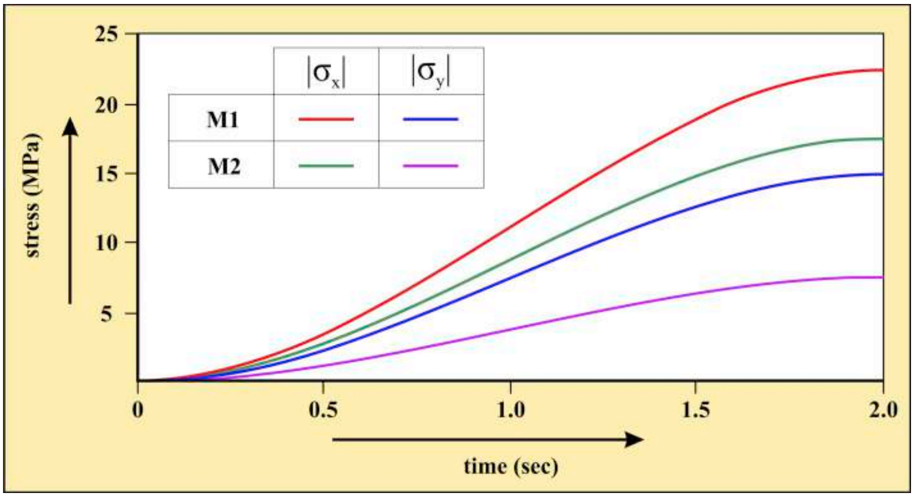

Fig. 10. The magnitude of the applied stresses, both normal and parallel to the layer boundaries, increase over an interval of 2 s $|\sigma_X|$and $|\sigma_Y|$rise from 0 to 22.5 MPa and 15 MPa for M1, whereas for M2 they increase from 0 to 17.5 MPa and 7.5 MPa.

place has a curvilinear geometry across the layer boundaries (Fig. 11p). This gives a 'false' impression that the fracture might have undergone refraction while propagating from the upper domain to the middle one. Moreover, the fracture originating from the notch ne1 in both M1-T and M1-TB make ~80° with the horizontal (Fig. 11c, l). But, for M1-A, fracture from the same notch is ~ perpendicular to the interlayer boundary (Fig. 11o). Hence, any apparent deflection of fractures propagating across layers presumably depends upon the location of impurities in the vicinity. The first principal strain axis (ε_1) does not re-orient across the layers except close to the notches (Fig. 12).

While approaching layer interfaces, fractures may face multiple consequences viz., termination, kinking, swerving, generating new fractures, propagation parallel to the interface etc. (Wu et al., 2004; Chang et al., 2015). Apart from the mechanical properties of the individual layers, horizontal stress disparity and shear strength at the interface also control the fracture propagation in layered materials (Daneshy, 1978; Teufel and Clark, 1981, 1984). A fracture may terminate while moving from low to high Young's modulus as the stress intensity at the crack-tip diminishes while approaching the interface (Simonson et al., 1978). Shear strength and frictional properties of the interface influences the migration of shear stress across the interface, whereas, a critical normal stress is required for fracture propagation across the interface (Teufel and Clark, 1981, especially their Fig. 2, Altammar et al., 2019). Although quantifying the shear strength and frictional properties of the studied domain interfaces are beyond the scope of this study, the mechanical micro-stratification (cleavage and microlithon domains) is clearly visible in the studied samples.

With reference to eqns (9)–(11), the locations with $Y_F \geq 0$ presumably overlap the zones of high (J_2) dev. stress and (J_2) elastic strain tensor (Figs. 11 and 13), which in turn have developed along the zones of high first principal stress (Fig. 13d,h,l,p,t). This also implies that fractures, under general shear regime, preferentially follow the zones of maximum compression ($\sigma_1 > 30$ MPa; Fig. 12d,h,l,p) in the vicinity of impurities/notches. In fact, on careful observation, the red zone (Fig. 13t) in the layer L_M shows a curved geometry remarkably resembling the fracture zone at the same location (Fig. 11o).

The case is a little more complex for M2. Irrespective of the location of the notches, fractures within the mica-rich domain (L_M) (Table- 1) exhibit two orientations viz. at high (>85°) and low (<20°) angles to the horizontal (Fig. 14). The angle between them exceeds 105°. In sandstone domains (L_T and L_B), however, only a single set of steeply dipping (~67–85°) fractures is prominent that possibly resemble R- and R′-shears (Pollard and Fletcher, 2005) (Fig. 14). But, we would rather refrain from stating this as an example of refraction because, even in the absence of impurities/notches in the domains L_T and L_B, the orientation of fractures in L_M (mica-rich layer) remains the same (Fig. 14d,e,f). Besides, fractures within L_M initiate even when the same has not propagated from the sandstone top and bottom domains (Fig. 14b,h,k). More importantly, it is observed that the initiation of high-angle fractures in L_M domain appears to influence the orientation of fractures in L_T and L_B. For example, in M2-B, at t = 1.5 and 1.75 s (Fig. 14g and h) the fractures originating from both ends of the notch ne3 are near-parallel and lie at ~70° to the horizontal axis. However, at t = 2.00 s (Fig. 14i), fractures initiating from the upper end (closer to L_M) of the notch ne3 makes ~ 87° (same as that of the high angle fracture in L_M) with horizontal axis.

The remainder observations from M2 resemble those from M1 i.e., the fractures develop at regions of high σ_1, ε_1, $(J_2)_{dev.\ stress}$, and $(J_2)_{elastic\ strain\ tensor}$ (Fig. 15). Similar to M1 models, the first principal strain axis does not re-orient across the layers in case of M2 models, except close to the notches (Fig. 16). However, there lies one disparity. In case of M2-M, fractured zones do not continue into L_T nor L_B (Fig. 14d–f) neither do the most strained zones (Fig. 15e). But, the zones of high σ_1 and $(J_2)_{dev.\ stress}$ not only continue into LT and LB, they re-orient (deep red zones in Fig. 14g and h). Consequently, the overall geometry and distribution of fractures within and across layers of contrasting rheology/competence is primarily guided by the magnitude of ε_1. The distribution of impurities in the rocks presumably plays a major role in the genesis of fractures and may confuse the viewer with a 'false' impression of refraction.

6. Discussions

Shear and low-grade metamorphism have presumably caused prominent inhomogeneity in the rheological configuration of the greywacke of the Rautgara Formation. We document shear-induced microfractures that refract at the boundaries between the cleavage- and microlithon-domains (c- and m-domains). In this study a total of 25 c-domains and 26 m-domains, from three natural micro-fractures have been analysed. Vorticity analysis in Bose et al. (2018) indicates 53% simple shear for the whole rock. This type of stress, referred as general shear/sub-simple shear/quasi simple shear/direct shear (Mandl, 1999), produces hybrid fractures having properties of both the shear- and extension fractures (Ramsey and Chester, 2004). Under microscope, minor drags of main foliation are observed at places along the fracture only when it crosses the relatively incompetent c-domains (Fig. 3c). However, no such drags of foliation/grain margins exist where the fracture cross-cuts quartz grains or relatively more competent m-domains (Fig. 3b). Absence of displacement indicates that these fractures

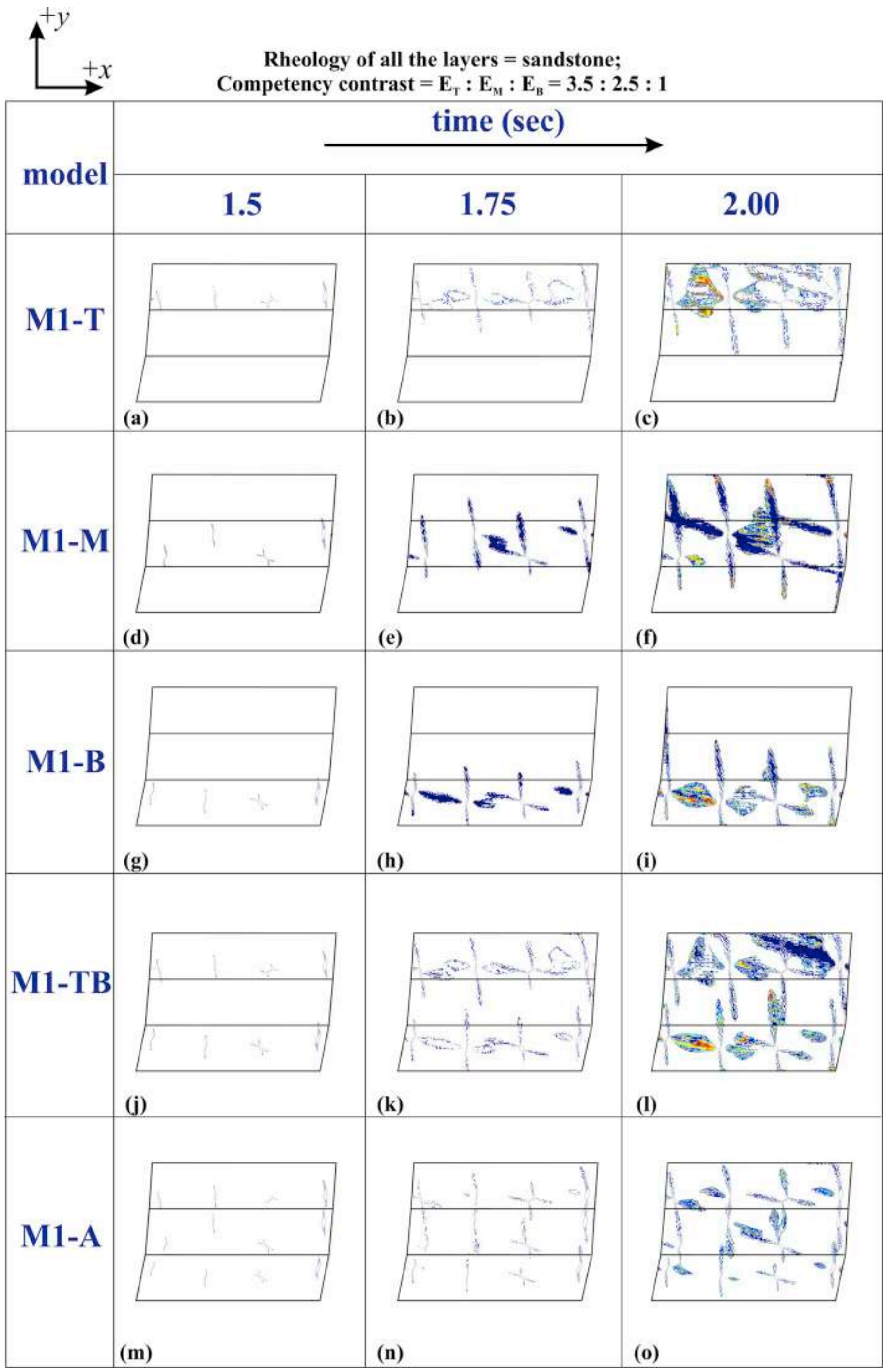

Fig. 11. Fracture zones ($Y_F \geq 0$) in model M1 E_T:E_M:E_B = 3.5:2.5:1; $|\sigma_X|$and $|\sigma_Y|$that vary from 0 to 22.5 MPa and 15 MPa, respectively from t = 0–2 s. Snapshots of the model results at t = 1.5, 1.75 and 2 s.

formed purely by extension without any shear components (Twiss and Moores, 2007). Previous works on fracture refraction through mechanically stratified layers (Ferrill et al., 2017a, b and references therein) indicate that the competent layers prefer tensile- or hybrid-cracks, whereas, shear failure is preferred in the incompetent layers. Recently, Carlini et al. (2019) report strike-slip faults from the Italian northern Apennines and provide the detailed mechanism for the initiation and propagation of fracture refraction. Some of our observations resemble theirs, viz., 1. vis-à-vis presence of shear- and tensile fracture, 2. abundance of clays in the mechanically weak domains, 3. strain analyses supporting a hybrid failure mode. The other aspects suggested by Carlini et al. (2019), specially the role played by fluid, remains a matter of future study. However, the observations made in current study (i.e., shear/hybrid fracture in c-domains and tensile fracture in m-domains) indicate the presence of micro-scale mechanical stratigraphy in the form of c- and m-domains.

Luo et al. (2019) report a ~ 90% decrease in Young's modulus corresponding to an increase from room temperature to 800 °C. Shear-induced heat (Mulchrone and Mukherjee, 2016; Mukherjee, 2017), might change Young's Modulus in microscale. Our models do not explore that possibility. The present models do not aim to recreate/incorporate all the observations made under an optical microscope. Rather, as

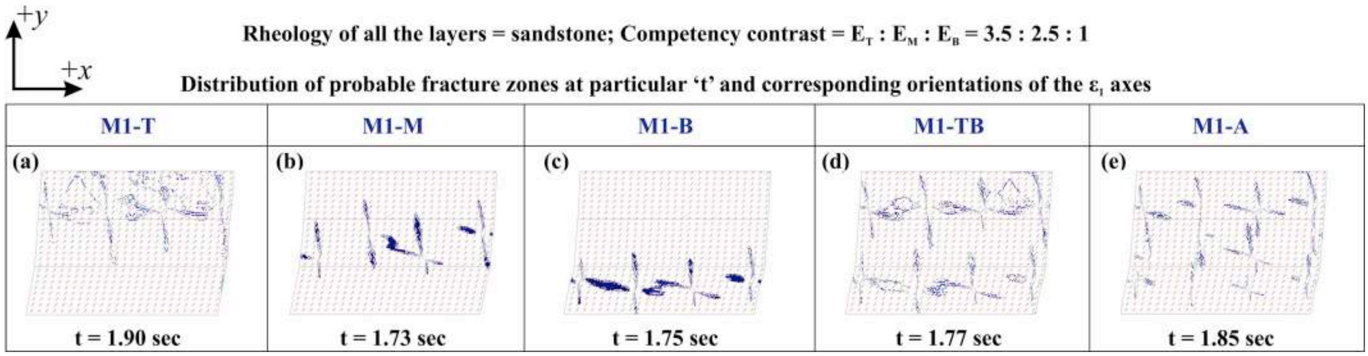

Fig. 12. Variation in the orientation of the maximum principal strain axis (ε_1) across the layers of model M1. Distribution of the fracture zones ($Y_F \geq 0$) at particular 't', which vary for different sub-groups of M1.

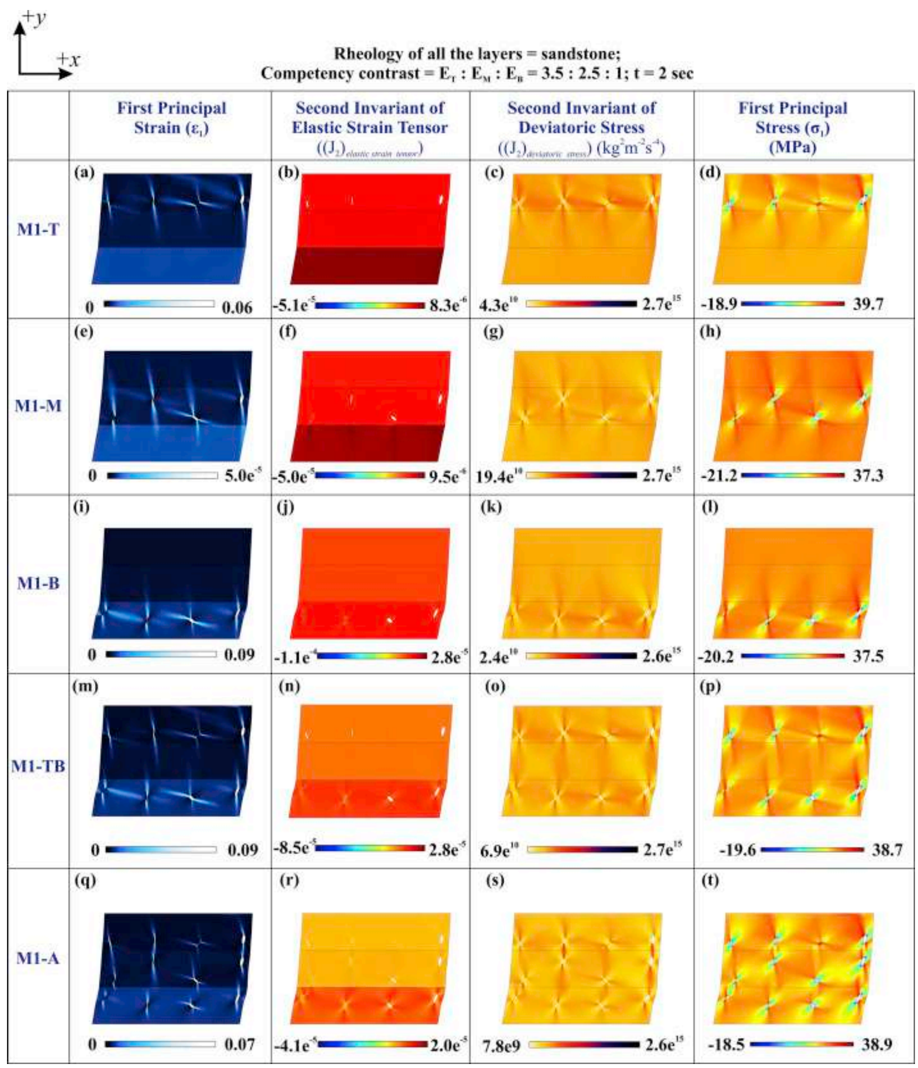

Fig. 13. Results for model M1 (E_T:E_M:E_B = 3.5:2.5:1; $|\sigma_X|$and$|\sigma_Y|$ vary from 0 to 22.5 MPa and 15 MPa, respectively from t = 0–2 s) showing the variations in the magnitude of first principal strain, second invariant of elastic strain tensor, second invariant of deviatoric stress and the first principal stress, at the end of t = 2 s. Note: $e^{10} = 10^{10}$. Thus, $4.3e^{10} = 4.3 \times 10^{10}$.

mentioned in Section. 5, they address the following: (i) fracture propagation and geometry across the layers, (ii) compare models with the natural examples, thereby to comment on (iii) how far competency contrast amongst layers matter. Mineral contents primarily decide viscosity of the layers and hence the degree of cleavage refraction (e.g. Treagus, 1983). Ratio of effective viscosity between the quartz layer and the phyllitic layer usually is < 10 (Czeck et al., 2019). Viscosities of rocks strongly depend on the temperature and hence their depth of occurrence below the ground surface (review in Mukherjee and Mulchrone, 2012; Mukherjee, 2013). The viscosity ratios referred in this work (Fig. 5) hold true for the time range when the fracture propagated through the rocks, which can differ from the present day viscosity ratio

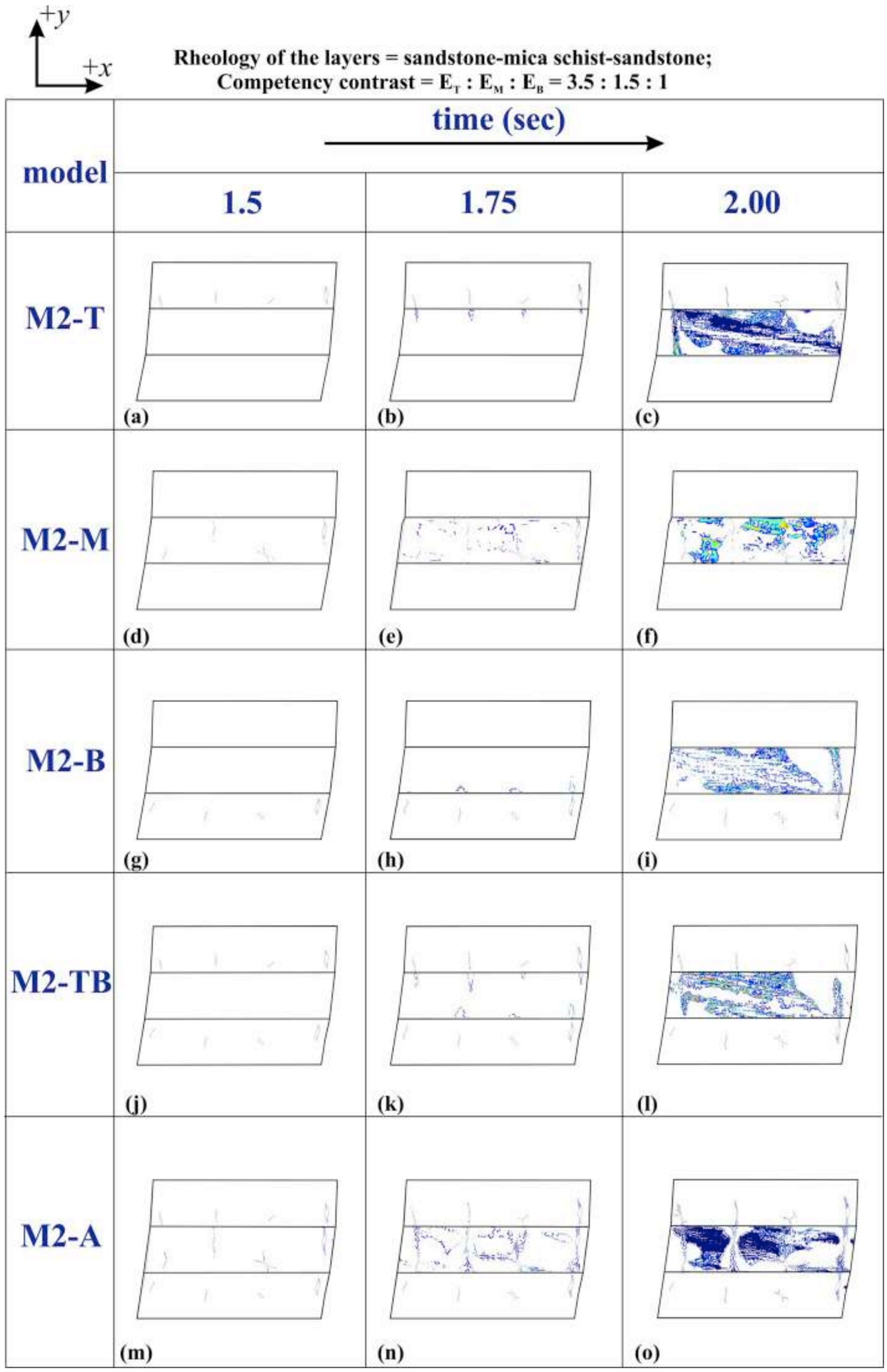

Fig. 14. Fracture zones ($Y_F \geq 0$) in model M2 E_T:E_M:E_B = 3.5:1.9:1; $|\sigma_X|$and$|\sigma_Y|$that vary from 0 to 17.5 MPa and 7.5 MPa, respectively from t = 0–2 s. Snapshots of the model results at t = 1.5, 1.75 and 2 s are shown.

between the two layers. Continuation of the present study can lead to predict how fractures and therefore fluids can migrate in a deforming or already deformed layered rock mass (e.g., Schöpfer et al., 2009).

7. Conclusions

In micro-scale a low-grade meta-sedimentary rock developed clay rich cleavage domains and quartz rich microlithon domains under the influences of shear deformation. Quartz-filled fractures refracts while passing through theses domains indicating inter-domain competence contrasts. Quantification of competence contrast has been done from the refraction angles. Although previously conducted strain analyses indicate a hybrid failure mode, there are co-existence of shear (in cleavage domains) and tensile fractures (in microlithon domains). These observations indicate the formation of shear-induced mechanical stratigraphy in micro-scale and justifies the applicability of fracture refraction as a tool to quantify the domain wise competence contrast. The numerical models reveal that closely spaced impurities may curve the possible fracture domains across the layer boundaries producing a ‘false’ impression of refraction.

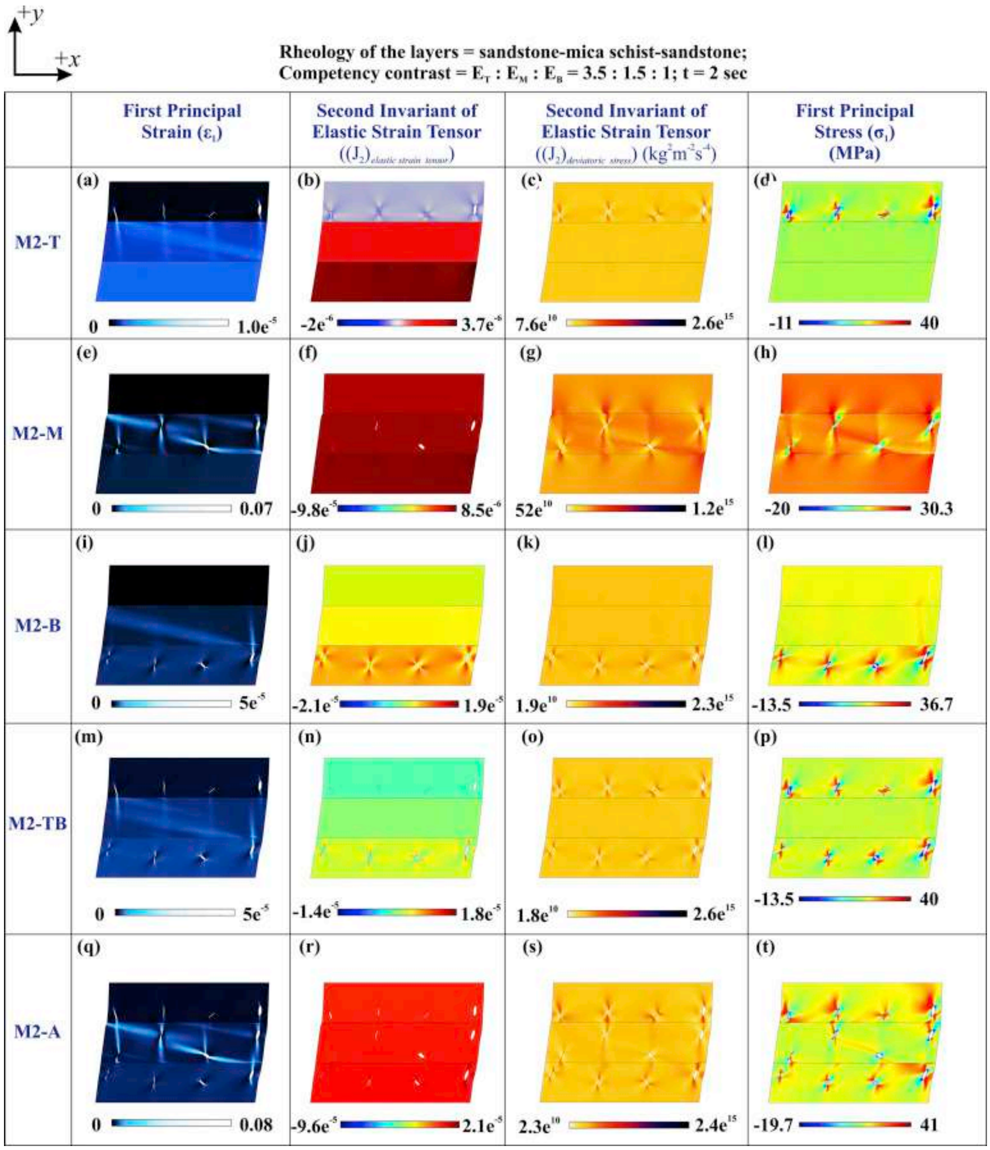

Fig. 15. Results for model M2 (E_T:E_M:E_B = 3.5:1.9:1; $|\sigma_X|$and$|\sigma_Y|$ vary from 0 to 17.5 MPa and 7.5 MPa, respectively from t = 0–2 s) showing the variations in the magnitude of first principal strain, second invariant of elastic strain tensor, second invariant of deviatoric stress and the first principal stress, at the end of t = 2 s. Note: e^{10} indicates 10^{10}. Thus, $4.3e^{10} = 4.3 \times 10^{10}$.

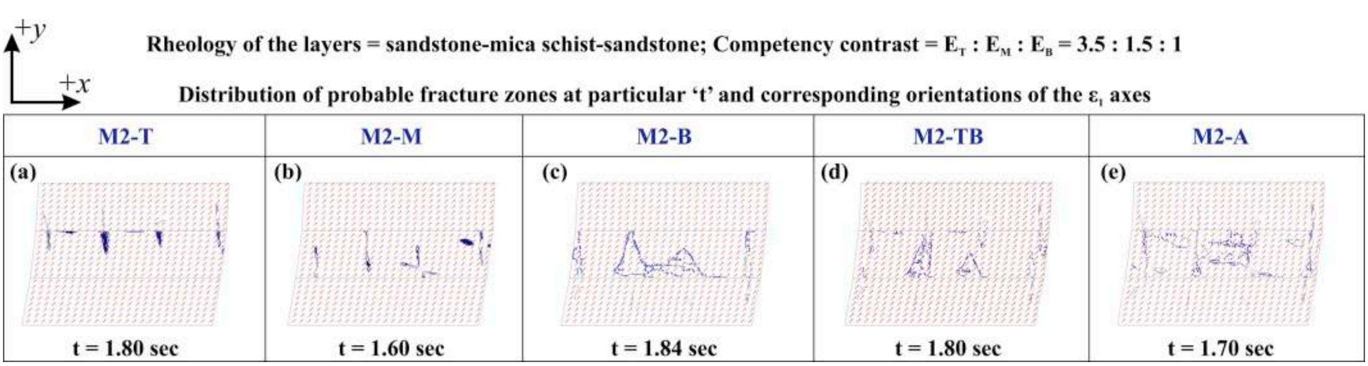

Fig. 16. Variation in the orientation of the maximum principal strain axis (ε_1) across the layers of model M2. Distribution of the fracture zones ($Y_F \geq 0$) at particular 't', which vary for different sub-groups of M2, are also shown.

Author contibution statement

NB studied the thin-sections, prepared the related diagrams and wrote the article substantially.

DD performed the numerical simmulations in COMSOL Multiphysics v5.4 and wrote the corresponding part of the article.

SM wrote a significant part of the article and revised drafts. Fieldwork was conducted by NB and SM.

Declaration of competing interest

Authors have no conflict of interest with anyone regarding this work.

Acknowledgements

Fieldwork was funded by IIT Bombay in terms of CPDA grant to SM. SM acknowledges the assistance in the lab done by the summer interns Shalaila Bhalla (Department of Earth Sciences, University of Toronto), Yash Rawat (Department of Earth Sciences, IIT Roorkee) and Shiba Nikalje (St Xaviers College, Mumbai). The authors extend their gratitude to the handling editor Ian Alsop and two anonymous reviewers.

Appendix A. Supplementary data

Supplementary data to this article can be found online at https://doi.org/10.1016/j.jsg.2020.103995.

Appendix. Symbols and their meanings

Symbol	Meaning
E	Young's modulus
E_{eff}	Effective Young's modulus
$\overline{E}$	Equivalent Young's modulus
E_T	Young's modulus for top layer
E_M	Young's modulus for middle layer
E_B	Young's modulus for bottom layer
ν	Poisson's ratio
ρ	Density
γ_m	Shear strain m-domain
γ_c	Shear strain c-domain
Θ_m	Angle between the fracture and the layer normal in m-domain
θ_c	Angle between the fracture and the layer normal in c-domain
σ_p	Peak differential stress
μ_m	Dynamic viscosity m-domain
μ_c	Dynamic viscosity m-domain
t	Time
u	Displacement vector
X, y	Spatial coordinates
X, Y	Material coordinates
F	Body force
σ_0	Initial stress state
ε_0	Initial strain state
ε_{th}	Thermal strain
σ_1	Maximum principal stress
σ_2	Intermediate principal stress
σ_3	Minimum principal stress
ε_1	Maximum principal strain
ε_2	Intermediate principal strain
ε_3	Minimum principal strain
μ_i	Coefficient of internal friction
J_2	Second invariant of a tensor
C	Cohesion
Y_F	Yield function
σ_x	Stress parallel to the x-axis
σ_y	Stress parallel to the y-axis
L_T	Top layer
L_M	Middle layer
L_B	Bottom layer
C_o	Unconfined compressive strength

References

Adams, J.W., Ruh, R., Mazdiyasni, K.S., 1997. Young's modulus, flexural strength, and fracture of yttria-stabilized zirconia versus temperature. J. Am. Ceram. Soc. 80, 903–908.
Agarwal, N.C., Kumar, G., 1973. Geology of the upper bhagirathi and yamuna valleys, uttarkashi district, kumaun Himalaya. Himal. Geol. 3, 2–23.
Agliardi, F., Zanchetta, S., Crosta, G.B., 2014. Fabric controls on the brittle failure of folded gneiss and schist. Tectonophysics 637, 150–162.
Alsop, G.I., Marco, S., 2014. Fold and fabric relationships in temporally and spatially evolving slump systems: a multi-cell flow model. J. Struct. Geol. 63, 27–49.
Alsop, G.I., Weinberger, R., Levi, T., Marco, S., 2016. Cycles of passive versus active diapirism recorded along an exposed salt wall. J. Struct. Geol. 84, 47–67.
Alsop, G.I., Weinberger, R., Marco, S., 2018a. Distinguishing thrust sequences in gravity-driven fold and thrust belts. J. Struct. Geol. 109, 99–119.

Alsop, G.I., Weinberger, R., Marco, S., Levi, T., 2018b. Fault and fracture patterns around a strike-slip influenced salt wall. J. Struct. Geol. 106, 103–124.
Alsop, G.I., Weinberger, R., Marco, S., Levi, T., 2019. Identifying soft-sediment deformation in rocks. J. Struct. Geol. 125, 248–255.
Altammar, M.J., Agrawal, S., Sharma, M.M., 2019. Effect of geological layer properties on hydraulic-fracture initiation and propagation: an experimental study. SPE J. https://doi.org/10.2118/184871-PA. SPE 184871.
Anders, L.H., Laubach, S.E., Scholz, C.H., 2014. Microfractures: a review. J. Struct. Geol. 69, 377–394.
Argles, T.W., 2010. Recording structural information. In: Coe, A.L. (Ed.), Geological Field Techniques. Wiley Blackwell, ISBN 978-1-4443-3061-8, pp. 163–191.
Austin, N.J., Kennedy, L.A., 2005. Textural controls on the brittle deformation of dolomite: variations in peak strength. In: Gapais, D., Brun, J.P., Cobbold, P.R. (Eds.), Deformation Mechanisms, Rheology and Tectonics: from Minerals to the Lithosphere, vol.243. Geological Society London Special Publications, pp. 37–49.
Aydin, A., Basu, A., 2005. The Schmidt hammer in rock material characterization. Eng. Geol. 81, 1–14.
Berry, J.P., 1960a. Some kinetic considerations of the Griffith criterion for fracture—I: equations of motion at constant force. J. Mech. Phys. Solid. 8, 194–206.
Berry, J.P., 1960b. Some kinetic considerations of the Griffith criterion for fracture—II: equations of motion at constant deformation. J. Mech. Phys. Solid. 8, 207–216.
Bose, N., Dutta, D., Mukherjee, S., 2018. Role of grain-size in phyllonitisation: insights from mineralogy, microstructures, strain analyses and numerical modeling. J. Struct. Geol. 112, 39–52.
Brown, M., 2005. One view of dynamic crustal rheology during orogenesis. In: AGU Fall Meeting Abstracts.
Bürgmann, R., Pollard, D.D., Martel, S.J., 1994. Slip distributions on faults: effects of stress gradients, inelastic deformation, heterogeneous host-rock stiffness, and fault interaction. J. Struct. Geol. 16, 1675–1690.
Carlini, M., Viola, G., Mattila, J., Castellucci, L., 2019. The role of mechanical stratigraphy on the refraction of strike-slip faults. Solid Earth 10, 343–356.
Célérier, J., Harrison, T.M., Webb, A.A.G., Yin, A., 2009. The kumaun and garwhal lesser Himalaya, India: Part 1. Structure and stratigraphy. Geol. Soc. Am. Bull. 121, 1262–1280.
Chang, X., Shan, Y., Zhang, Z., Tang, C., Ru, Z., 2015. Behavior of propagating fracture at bedding interface in layered rocks. Eng. Geol. 197, 33–41.
Colmenares, L.B., Zoback, M.D., 2002. A statistical evaluation of intact rock failure criteria constrained by polyaxial test data for five different rocks. Int. J. Rock Mech. Min. Sci. 39, 695–729.
Czeck, D.M., Traut, J.T., Hudleston, P.J., 2019. Rheological information determined from cleavage refraction in naturally deformed interlayered quartzites and phyllites. In: Bond, C.E., Lebit, H.D. (Eds.), Folding and Fracturing of Rocks: 50 Years of Research since the Seminal Text Book of J. G. Ramsay. Geological Society, London, Special Publications, p. 487. https://doi.org/10.1144/SP487-2018-49. First published online 19 March 2019.
Damasceno, D.R., Eckert, A., Liu, X., 2017. Flexural-slip during visco-elastic buckle folding. J. Struct. Geol. 100, 62–76.
Daneshy, A.A., 1978. Hydraulic fracture propagation in layered formations. Soc. Petrol. Eng. J. 18, 33–41.
Dennis, J.G., 1987. Structural Geology: An Introduction. William C Brown Publication. ISBN-10: 0697001334.
Dubey, A.K., 2014. Understanding an Orogenic Belt. Springer, Switzerland, p. 401.
Eberhardt, E., Stimpson, B., Stead, D., 1999. Effects of grain size on the initiation and propagation thresholds of stress-induced brittle fractures. Rock Mech. Rock Eng. 32, 81–99.
Eyinla, D.S., Oladunjoye, M.A., 2014. Estimating geo-mechanical strength of reservoir rocks from well logs for safety limits in sand-free production. J. Environ. Earth Sci. 4, 38–43.
Ferrill, D.A., Morris, A.P., 2003. Dilational normal faults. J. Struct. Geol. 25, 183–196.
Ferrill, D.A., Morris, A.P., Mcginnis, R.N., Smart, K.J., 2016. Myths about normal faulting. In: Childs, C., Holdsworth, R.E., Jackson, C.A.-L., Manzocchi, T., Walsh, J. J., Yielding, G. (Eds.), The Geometry and Growth of Normal Faults, vol.439. Geological Society, London, Special Publications, pp. 41–56.
Ferrill, D.A., Evans, M.A., McGinnis, R.N., Morris, A.P., Smart, K.J., Wigginton, S.S., Gulliver, K.D.H., Lehrmann, D., Zoeten, E., Sickmann, Z., 2017a. Fault zone processes in mechanically layered mudrock and chalk. J. Struct. Geol. 97, 118–143.
Ferrill, D.A., Morris, A.P., McGinnis, R.N., Smart, K.J., Wigginton, S.S., Hill, N.J., 2017b. Mechanical stratigraphy and normal faulting. J. Struct. Geol. 94, 275–302.
Fossen, H., 2016. Structural Geology, second ed. Cambridge University Press, ISBN 978-1-107-05764-7, p. 293.
Gerya, T., 2010. Introduction to Numerical Geodynamic Modelling. Cambridge University Press, Cambridge, p. 345. ISBN-13: 978-0521887540.
Goodman, R.E., 1980. Introduction to Rock Mechanics. Volume 2. John Wiley & sons, New York, p. 576. ISBN-13: 978-8126525669.
Grasemann, B., Fritz, H., Vannay, J.-C., 1999. Quantitative kinematic flow analysis from the Main Central Thrust zone (NW Himalaya, India); Implications for a decelerating strain path and the extrusion of orogenic wedges. J. Struct. Geol. 21, 837–853.
Groome, W.G., Johnson, S.E., 2006. Constraining the relative strengths of high-grade metamorphic rocks using foliation refraction angles: an example from the Northern New England Appalachians. J. Struct. Geol. 28, 1261–1276.
Gross, M.R., Fischer, M.P., Engelder, T., Greenfield, R.J., 1995. Factors controlling joint spacing in interbedded sedimentary rocks: interpreting numerical models with field observations from the Monterey Formation, USA. In: Ameen, M.S. (Ed.), Fractography: Fracture Topography as a Tool in Fracture Mechanics and Stress Analysis, vol.92. Geological Society of London Special Publications, pp. 215–233.
Gudmundsson, A., 2011. Rock Fractures in Geological Processes. Cambridge University Press, Cambridge, ISBN 9780511975684, p. 578.
Haimson, B., Chang, C., Ma, X., 2017. True triaxial testing of rocks and the effect of the intermediate principal stress on failure characteristics. In: Teng Feng, X. (Ed.), Rock Mechanics and Engineering Volume 1: Principles, pp. 379–395.
Hancock, P.L., 1985. Brittle microtectonics: principles and practice. J. Struct. Geol. 7, 437–457.
Helmstaedt, H., Greggs, R.G., 1980. Stylolitic cleavage and cleavage refraction in lower Paleozoic carbonate rocks of the Great Valley, Maryland. Tectonophysics 66 (1–3), 99–114.
Henderson, P., Henderson, G.M., 2009. The Cambridge Handbook of Earth Science Data. Cambridge University Press, Cambridge, p. 277. ISBN-13: 978-0521693172.
Henk, A., Nemčok, M., 2008. Stress and fracture prediction in inverted half-graben structures. J. Struct. Geol. 30, 81–97.
Hooker, J.N., Laubach, S.E., Marrett, R., 2018. Microfracture spacing distributions and the evolution of fracture patterns in sandstones. J. Struct. Geol. 108, 66–79.
Huang, K.P., Chang, K.J., Wang, T.T., Jeng, F.S., 2010. Buckling folds of a single layer embedded in matrix–Folding behavior revealed by numerical analysis. J. Struct. Geol. 32, 960–974.
Jaeger, J.C., Cook, N.G., Zimmerman, R., 2009. Fundamentals of Rock Mechanics, fourth ed. Blackwell Publishing, Malden, ISBN 978-0-632-05759-7, p. 475.
Jain, A.K., 1971. Stratigraphy and tectonics of lesser himalayan region of uttarkashi, garhwal Himalaya. Himal. Geol. 1, 25–58.
Jeng, F.S., Huang, K.P., 2008. Buckling folds of a single layer embedded in matrix–Theoretical solutions and characteristics. J. Struct. Geol. 30, 633–648.
Johnson, S.E., Lenferink, H.J., Price, N.A., Marsh, J.H., Koons, P.O., West, D.P., Beane, R., 2009. Clast-based kinematic vorticity gauges: the effects of slip at matrix/clast interfaces. J. Struct. Geol. 31, 1322–1339.
Justo, J., Castro, J., Cicero, S., Sánchez-Carro, M.A., Husillos, R., 2017. Notch effect on the fracture of several rocks: application of the theory of critical distances. Theor. Appl. Fract. Mech. 90, 251–258.
Kanagawa, K., 1993. Competence contrasts in ductile deformation as illustrated from naturally deformed chert-mudstone layers. J. Struct. Geol. 15, 865–885.
Karato, S.I., 2008. Deformation of Earth Materials: an Introduction to the Rheology of Solid Earth. Cambridge University Press, Cambridge, ISBN 9780511804892, p. 462.
Katz, O., Reches, Z., Roegiers, J.C., 2000. Evaluation of mechanical rock properties using a Schmidt Hammer. Int. J. Rock Mech. Min. Sci. 37, 723–728.
Katz, O., Reches, Z.E., Baer, G., 2003. Faults and their associated host rock deformation: Part I. Structure of small faults in a quartz–syenite body, southern Israel. J. Struct. Geol. 25, 1675–1689.
Kenis, I., Urai, J.L., Sintubin, M., 2006. The development of bone-shaped structures in initially segmented layers during layer-parallel extension: numerical modelling and parameter sensitivity analysis. J. Struct. Geol. 28, 1183–1192.
Kipp, M.E., Grady, D.E., Chen, E.P., 1980. Strain-rate dependent fracture initiation. Int. J. Fract. 16, 471–478.
Koehn, D., Arnold, J., Passchier, C.W., 2005. Fracture and vein patterns as indicators of deformation history: a numerical study. In: Gapais, D., Brun, J.P., Cobbold, P.R. (Eds.), Deformation Mechanisms, Rheology and Tectonics: from Minerals to the Lithosphere, vol.243. Geological Society London Special Publications, pp. 11–24.
Kopp, M.L., Leonov, Y.G., Adzhamyan, Z., 1994. Deformation of west Arabian plate due to strike-slip movements along the Levant fault. Geotectonics 28, 238–253.
Lo, S.H., 2015. Finite Element Mesh Generation. Taylor & Francis Group, Boca Raton, ISBN 9781138749245, p. 618.
Luo, N., Liang, H., Shen, T., Yang, W., 2019. Temperature dependence of Young's modulus of red sandstone. Therm. Sci. 23, 1599–1606.
Maccaferri, F., Bonafede, M., Rivalta, E., 2010. A numerical model of dyke propagation in layered elastic media. Geophys. J. Int. 180, 1107–1123.
Maillot, B., Koyi, H., 2006. Thrust dip and thrust refraction in fault-bend folds: analogue models and theoretical predictions. J. Struct. Geol. 28, 36–49.
Mandl, G., 1999. Faulting in Brittle Rocks: an Introduction to the Mechanics of Tectonic Faults. Springer Science & Business Media.
Manoharan, M., Lewandowski, J.J., 1990. Crack initiation and growth toughness of an aluminum metal-matrix composite. Acta Metall. Mater. 38, 489–496.
Marques, F.O., Taborda, R., Bose, S., Antunes, J., 2005. Effects of confinement on matrix flow around a rigid inclusion in viscous simple shear: insights from analogue and numerical modelling. J. Struct. Geol. 27, 379–396.
McGinnis, R.N., Ferrill, D.A., Morris, A.P., Smart, K.J., Lehrmann, D., 2017. Mechanical stratigraphic controls on natural fracture spacing and penetration. J. Struct. Geol. 95, 160–170.
McNamara, D.D., Faulkner, D., McCarney, E., 2014. Rock properties of greywacke basement hosting geothermal reservoirs, New Zealand: preliminary results. In: Proceedings of the 39th Workshop on Geothermal Reservoir Engineering at Stanford University, California, USA, pp. 1067–1076. SGP-TR-202.
Mecholsky, J.J., Freimam, S.W., Rice, R.W., 1976. Fracture surface analysis of ceramics. J. Mater. Sci. 11, 1310–1319.
Meyer, S.E., Kaus, B.J., Passchier, C., 2017. Development of branching brittle and ductile shear zones: a numerical study. G-cubed 18, 2054–2075.
Mielke, P., Weinert, S., Bignall, G., Sass, I., 2016. Thermo-physical rock properties of greywacke basement rock and intrusive lavas from the Taupo Volcanic Zone, New Zealand. J. Volcanol. Geoth. Res. 324, 179–189.
Mogi, K., 2007. Experimental Rock Mechanics. Taylor & Francis Group, London, ISBN 9780415394437, p. 361.
Mukherjee, S., 2013. Channel flow extrusion model to constrain dynamic viscosity and Prandtl number of the Higher Himalayan Shear Zone. Int. J. Earth Sci. 102, 1811–1835.

Mukherjee, S., 2014. Atlas of Shear Zone Structures in Meso-Scale. Springer Geology, ISBN 978-3-319-00088-6, p. 124.
Mukherjee, S., 2017. Shear heating by translational brittle reverse faulting along a single, sharp and straight fault plane. J. Earth Syst. Sci. 126, 1–5.
Mukherjee, S., Mulchrone, K., 2012. Estimating the viscosity and Prandtl number of the tso morari gneiss dome, western Indian Himalaya. Int. J. Earth Sci. 101, 1929–1947.
Mulchrone, K.F., Mukherjee, S., 2016. Kinematics and shear heat pattern of ductile simple shear zones with 'slip boundary condition'. Int. J. Earth Sci. 105, 1015–1020.
Nasseri, M.H.B., Rao, K.S., Ramamurthy, T., 2003. Anisotropic strength and deformational behavior of Himalayan schists. Int. J. Rock Mech. Min. Sci. 40, 3–23.
Nespoli, M., Belardinelli, M.E., Bonafede, M., 2019. Fault dip variations related to elastic layering. Geophys. J. Int. 220, 1095–1111.
Nevin, C.M., 1949. Principles of Structural Geology, fourth ed. John Wiley & Sons Inc., New York.
Pan, P.Z., Feng, X.T., Hudson, J.A., 2012. The influence of the intermediate principal stress on rock failure behaviour: a numerical study. Eng. Geol. 124, 109–118.
Pant, P.D., Chauhan, R., Bhakuni, S.S., 2012. Development of transverse fault along North Almora Thrust, Kumaun Lesser Himalaya, India: a study based on field and magnetic fabrics. J. Geol. Soc. India 79, 429–448.
Peacock, D.C.P., Sanderson, D.J., 1992. Effects of layering and anisotropy on fault geometry. J. Geol. Soc. 149, 793–802.
Pollard, D.D., Fletcher, R.C., 2005. Fundamentals of Structural Geology. Cambridge University Press, Cambridge, p. 500. ISBN-13: 978-0521839273.
Price, N.J., Cosgrove, J.W., 1990. Analysis of Geological Structures. Cambridge University Press, Cambridge, pp. 453–458. ISBN-13 978-0-521-26581-2.
Qi, L., Chen, H., Chen, Y., 2018. Tensor Eigenvalues and Their Applications. Springer Nature, Singapore, p. 329.
Ragan, D.M., 2009. Structural Geology: an Introduction to Geometrical Techniques, fourth ed. Cambridge University Press, p. 402. ISBN-13 978-0-521-89758-7.
Ramsey, J.M., Chester, F.M., 2004. Hybrid fracture and the transition from extension fracture to shear fracture. Nature 428, 63.
Schöpfer, M.P.J., Childs, C., Walsh, J.J., 2009. Two-dimensional Distinct Element Method (DEM) modeling of tectonic fault growth in mechanically layered sequences. In: Kolymbas, D., Viggiani, G. (Eds.), Mechanics of Natural Solids. Springer, ISBN 978-3-642-03578-4, pp. 127–146.
Shovkun, I., Espinoza, D.N., 2019. Fracture propagation in heterogeneous porous media: pore-scale implications of mineral dissolution. Rock Mech. Rock Eng. 1–15.
Simonson, E.R., Abou-Sayed, A.S., Clifton, R.J., 1978. Containment of massive hydraulic fractures. Soc. Petrol. Eng. J. 18, 27–32.
Takahashi, T., Tanaka, S., 2017. Compressive strength–seismic velocity relationship for sedimentary rocks. In: Ting-Feng, X. (Ed.), Rock Mechanics and Engineering Volume 1: Principles. Taylor & Francis Group, London, pp. 299–322.
Teufel, L.W., Clark, J.A., 1981. Hydraulic-fracture Propagation in Layered Rock: Experimental Studies of Fracture Containment (No. SAND-80-2219C; CONF-810518-7). Sandia National Labs., Albuquerque, NM (USA).
Teufel, L.W., Clark, J.A., 1984. Hydraulic fracture propagation in layered rock: experimental studies of fracture containment. Soc. Petrol. Eng. J. 24, 19–32.
Treagus, S.H., 1973. Buckling stability of a viscous single-layer system, oblique to the principal compression. Tectonophysics 19, 271–289.
Treagus, S.H., 1983. A theory of finite strain variation through contrasting layers, and its bearing on cleavage refraction. J. Struct. Geol. 5, 351–368.
Treagus, S.H., 1988. Strain refraction in layered systems. J. Struct. Geol. 10, 517–527.
Treagus, S.H., 1999. Are viscosity ratios of rocks measurable from cleavage refraction? J. Struct. Geol. 21, 895–901.
Tsuchiya, T., Hirata, M., Chiba, N., 2005. Young's modulus, fracture strain, and tensile strength of sputtered titanium thin films. Thin Solid Films 484, 245–250.
Twiss, R.J., Moores, E.M., 2007. Structural Geology. W.H. Freeman and Company, New York, p. 736. ISBN-13 978-0-7167-4951-6.
Valdiya, K.S., 1980. Geology of Kumaun Lesser Himalaya. Wadia Institute of Himalayan Geology, Dehradun, p. 291.
Vannay, J.C., Grasemann, B., 2001. Himalayan inverted metamorphism and syn-convergence extension as a consequence of a general shear extrusion. Geol. Mag. 138, 253–276.
Virgo, S., Abe, S., Urai, J.L., 2016. The influence of loading conditions on fracture initiation, propagation, and interaction in rocks with veins: results from a comparative Discrete Element Method study. J. Geophys. Res.: Solid Earth 121, 1730–1738.
Wall, O., 2002. Numerical modelling of fracture initiation in large steel specimens at impact. Eng. Fract. Mech. 69, 851–863.
Watkins, H., Bond, C.E., Cawood, A.J., Cooper, M.A., Warren, M.J., 2019. Fracture distribution on the Swift Reservoir Anticline, Montana: implications for structural and lithological controls on fracture intensity. In: Bond, C.E., Lebit, H.D. (Eds.), Folding and Fracturing of Rocks: 50 Years of Research since the Seminal Text Book of J. G. Ramsay, vol.487. Geological Society, London, Special Publications, pp. SP487–S489. https://doi.org/10.1144/SP487.9.
Weiss, L.E., 1972. The Minor Structures of Deformed Rocks: A Photographic Atlas. Springer-Verlag, Berlin, ISBN 978-3-642-48611-1.
Wu, H., Chudnovsky, A., Dudley, J.W., Wong, G.K., 2004. A map of fracture behavior in the vicinity of an interface. In: Gulf Rocks 2004, the 6th North America Rock Mechanics Symposium (NARMS). American Rock Mechanics Association. ARMA-04-620.
Zhang, P., Li, X.B., Li, N., 2008. Strength evolution law of cracked rock based on localized progressive damage model. J. Cent. S. Univ. Technol. 15, 493–497.